

arise from the attempt to interpret complex behaviour within the limits of a favoured structure. The main conclusions drawn from the present first-principles quantum simulations, together with those of ref. 23, are in accordance with a model that is deduced from, and is claimed to be consistent with, all known experimental data³³. □

Received 12 August; accepted 9 November 1998.

1. de Grothuss, C. J. T. Sur la décomposition de l'eau et des corps qu'elle tient en dissolution à l'aide de l'électricité galvanique. *Ann. Chim.* **LVIII**, 54–74 (1806).
2. Atkins, P. W. *Physical Chemistry* 6th edn, Ch. 24.8, 741 (Oxford Univ. Press, 1998).
3. Hückel, E. Theorie der Beweglichkeiten des Wasserstoff- und Hydroxylions in wässriger Lösung. *Z. Elektrochem.* **34**, 546–562 (1928).
4. Stearn, A. E. & Eyring, J. The deduction of reaction mechanisms from the theory of absolute rates. *J. Chem. Phys.* **5**, 113–124 (1937).
5. Bernal, J. D. & Fowler, R. H. A theory of water and ionic solution, with particular reference to hydrogen and hydroxyl ions. *J. Chem. Phys.* **1**, 515–548 (1933).
6. Wannier, G. Die Beweglichkeit des Wasserstoff- und Hydroxylions in wässriger Lösung. *Ann. Phys. (Leipzig)* **24**, 545–590 (1935).
7. Huggins, M. L. Hydrogen bridges in ice and liquid water. *J. Phys. Chem.* **40**, 723–731 (1936).
8. Wicke, E., Eigen, M. & Ackermann, Th. Über den Zustand des Protons (Hydroniumions) in wässriger Lösung. *Z. Phys. Chem. (N.F.)* **1**, 340–364 (1954).
9. Eigen, M. Proton transfer, acid–base catalysis and enzymatic hydrolysis. *Angew. Chem. Int. Edn Engl.* **3**, 1–19 (1964).
10. Zundel, G. & Metzger, H. Energiebänder der tunnelnden Überschuss-Protonen in flüssigen Säuren. Eine IR-spektroskopische Untersuchung der Natur der Gruppierungen $H_3O_2^+$. *Z. Physik. Chem. (N.F.)* **58**, 225–245 (1968).
11. Zundel, G. in *The Hydrogen Bond—Recent Developments in Theory and Experiments. II. Structure and Spectroscopy* (eds Schuster, P., Zundel, G. & Sandorfy, C.) 683–766 (North-Holland, Amsterdam, 1976).
12. Marx, D. & Parrinello, M. Ab initio path-integral molecular dynamics. *Z. Phys. B (Rapid Note)* **95**, 143–144 (1994).
13. Marx, D. & Parrinello, M. Ab initio path integral molecular dynamics: basic ideas. *J. Chem. Phys.* **104**, 4077–4082 (1996).
14. Tuckerman, M. E., Marx, D., Klein, M. L. & Parrinello, M. Efficient and general algorithms for path integral Car–Parrinello molecular dynamics. *J. Chem. Phys.* **104**, 5579–5588 (1996).
15. Cleland, W. W. & Kreevoy, M. M. Low-barrier hydrogen bonds and enzymic catalysis. *Science* **264**, 1887–1890 (1994).
16. Tuckerman, M. E., Marx, D., Klein, M. L. & Parrinello, M. On the quantum nature of the shared proton in hydrogen bonds. *Science* **275**, 817–820 (1997).
17. Guissani, Y., Guillot, B. & Bratos, S. The statistical mechanics of the ionic equilibrium of water: a computer simulation study. *J. Chem. Phys.* **88**, 5850–5856 (1988).
18. Halley, J. W., Rustad, J. R. & Rahman, A. A polarizable, dissociating molecular dynamics model for liquid water. *J. Chem. Phys.* **98**, 4110–4119 (1993).
19. Tuñón, I., Silla, E. & Bertrán, J. Proton solvation in liquid water. An ab initio study using the continuum model. *J. Phys. Chem.* **97**, 5547–5552 (1993).
20. Laria, D., Ciccotti, G., Ferrario, M. & Kapral, R. Activation free energy for proton transfer in solution. *Chem. Phys.* **180**, 181–189 (1994).
21. Komatsuzaki, T. & Ohmine, I. Energetics of proton transfer in liquid water. I. Ab initio study for origin of many-body interaction and potential energy surfaces. *Chem. Phys.* **180**, 239–269 (1994).
22. Wei, D. & Salathub, D. R. Hydrated proton clusters and solvent effects on the proton transfer barrier: a density functional study. *J. Chem. Phys.* **101**, 7633–7643 (1994).
23. Tuckerman, M., Laasonen, K., Sprik, M. & Parrinello, M. Ab initio molecular dynamics simulation of the solvation and transport of H_3O^+ and OH^- ions in water. *J. Phys. Chem.* **99**, 5749–5752 (1995); Ab initio molecular dynamics simulation of the solvation and transport of hydronium and hydroxyl ions in water. *J. Chem. Phys.* **103**, 150–161 (1995).
24. Lobaugh, J. & Voth, G. A. The quantum dynamics of an excess proton in water. *J. Chem. Phys.* **104**, 2056–2069 (1996).
25. Ando, K. & Hynes, J. T. Molecular mechanism of HCl acid ionization in water: ab initio potential energy surfaces and Monte Carlo simulations. *J. Phys. Chem. B* **101**, 10464–10478 (1997).
26. Schmidt, R. G. & Brickmann, J. Molecular dynamics simulation of the proton transport in water. *Ber. Bunsenges. Phys. Chem.* **101**, 1816–1827 (1997).
27. Sagnella, D. E. & Tuckerman, M. E. An empirical valence bond model for proton transfer in water. *J. Chem. Phys.* **108**, 2073–2083 (1998).
28. Vuilleumier, R. & Borgis, D. Quantum dynamics of an excess proton in water using an extended empirical valence-bond hamiltonian. *J. Phys. Chem. B* **102**, 4261–4264 (1998).
29. Schmitt, U. W. & Voth, G. A. Multistate empirical valence bond model for proton transport in water. *J. Phys. Chem. B* **102**, 5547–5551 (1998).
30. Billeter, S. R. & van Gunsteren, W. F. Protonizable water model for quantum dynamical simulations. *J. Phys. Chem. A* **102**, 4669–4678 (1998).
31. Kochanski, E., Kelterbaum, R., Klein, S., Rohmer, M. M. & Rahmouni, A. Decades of theoretical work on protonated hydrates. *Adv. Quantum Chem.* **28**, 273–291 (1997).
32. Benoit, M., Marx, D. & Parrinello, M. Tunneling and zero-point motion in high-pressure ice. *Nature* **392**, 258–261 (1998).
33. Agmon, N. The Grothuss mechanism. *Chem. Phys. Lett.* **244**, 456–462 (1995); Hydrogen bonds, water rotation and proton mobility. *J. Chim. Phys. Phys.-Chim. Biol.* **93**, 1714–1736 (1996).
34. Becke, A. D. Density-functional exchange-energy approximation with correct asymptotic behavior. *Phys. Rev. A* **38**, 3098–3100 (1988).
35. Lee, C., Wang, W. & Parr, R. G. Development of the Colle–Salvetti correlation-energy formula into a functional of the electron density. *Phys. Rev. B* **37**, 785–789 (1988).
36. Troullier, N. & Martins, J. L. Efficient pseudopotentials for plane-wave calculations. *Phys. Rev. B* **43**, 1993–2006 (1991).
37. Sprik, M., Hutter, J. & Parrinello, M. Ab initio molecular dynamics simulation of liquid water: comparison of three gradient-corrected density functionals. *J. Chem. Phys.* **105**, 1142–1152 (1996).
38. Ojamäe, L., Shavitt, I. & Singer, S. J. Potential models for simulations of the solvated proton in water. *J. Chem. Phys.* **109**, 5547–5564 (1998).

Acknowledgements. We thank K.-D. Kreuer for discussions. The calculations were performed on the Cray-T3E/816 of the Max-Planck-Gesellschaft.

Correspondence and requests for materials should be addressed to D.M. (e-mail: marx@pr.mpi-stuttgart.mpg.de).

Discrete alternating hotspot islands formed by interaction of magma transport and lithospheric flexure

Christoph F. Hieronymus* & David Bercovic†

* Danish Lithosphere Centre, Øster Voldgade 10 L, 1350 Copenhagen K, Denmark

† Department of Geology and Geophysics, University of Hawaii, Honolulu, Hawaii 96822, USA

The large-scale geometry and age progression of many hotspot island chains, such as the Hawaiian–Emperor chain, are well explained by the steady movement of tectonic plates over stationary hotspots. But on a smaller scale, hotspot tracks are composed of discrete volcanic islands whose spacing correlates with lithospheric thickness¹. Moreover, the volcanic shields themselves are often not positioned along single lines, but in more complicated patterns, such as the dual line known as the Kea and Loa trends of the Hawaiian islands^{2,3}. Here we make use of the hypothesis that island spacing is controlled by lithospheric flexure¹ to develop a simple nonlinear model coupling magma flow, which feeds volcanic growth, to the flexure caused by volcanic loads on the underlying plate. For a steady source of melt underneath a moving lithospheric plate, magma is found to reach the surface and build a chain of separate volcanic edifices with realistic spacing. If a volcano is introduced away from the axis of the chain, as might occur following a change in the direction of plate motion, the model perpetuates the asymmetry for long distances and times, thereby producing an alternating series of edifices similar to that observed in the Kea and Loa trends of the Hawaiian island chain.

Various models have been proposed to explain the formation of discrete islands within hotspot tracks. Periodicity in island formation may originate in the mantle by solitary waves^{4,5} on, or shear instabilities^{6,7} of, mantle plumes; these models, however, do not explain the observed correlation¹ between island spacing λ and lithospheric thickness H , that is, $\lambda \propto H^{3/4}$. Alternatively, stresses in the lithosphere may generate joints with regular spacing of the order of the thickness of the lithosphere with volcanic eruptions occurring at their intersections⁸; however, the stresses necessary to cause the observed pattern of volcanoes are not well constrained and may require multiple, somewhat *ad hoc*, origins⁸. Our model instead builds on the idea (motivated by the observed correlation between λ and H) that magma flow occurs at locations where the horizontal flexural stresses due to existing islands are approximately zero¹ (that is, at the transition between the flexural depression and the flexural bulge). The model provides a simplified yet self-consistent dynamical system that generates realistic results by taking into account the effects of flexural stresses and erosion of the dyke walls on fracture formation.

The physical processes involved in our model act on greatly varying length and time scales. Whereas the flexural wavelength is of the order of 100 km (ref. 9), and the flexural amplitude changes over timescales of volcano formation ($\sim 10^6$ years; ref. 10), a typical magma-transporting fracture is only 1–10 m wide and forms over timescales of days (ref. 11). A practical approach to treating this disparity in scales is to define the lithosphere's permeability to magma percolation as a continuous field variable, thus treating the average effects of fractures in a continuum mechanical sense. By analogy with the physics of fracture formation and evolution, the permeability is assumed to depend on stresses^{11,12} and total erosion (for example, melting^{13,14} and thermomechanical erosion¹⁵) of the fracture walls.

We first assume that the stresses influencing the permeability are due to both an impinging mantle plume, and lithospheric flexure (Fig. 1). The net effect of the plume on the base of the lithosphere is represented as a tensile stress or over-pressurization (due to inflation of the hotspot swell, horizontal spreading of the plume top, and/or high pressure of the melt region) of super-gaussian¹⁶ shape placed in the frame of reference of a lithosphere moving with velocity v in the negative x -direction:

$$\sigma_p(x, y, t) = Ae^{-\left[\frac{(x-vt)^2+y^2}{r^2}\right]^p} \quad (1)$$

Here A is the maximum stress, and r is the half-width of the source; p provides generality by allowing σ_p any shape, from purely gaussian ($p = 1$) to plateau-shaped ($p \gg 1$).

The stresses associated with plate flexure are assumed to be primarily a function of the surface load as described in thin-plate theory; the vertical deflection w caused by a load of height h (which is variable in space and time) and density ρ_m is therefore given by

$$D\nabla_h^4 w + (\rho_a - \rho_w)gw = -\rho_m gh \quad (2)$$

where D is the flexural rigidity⁹, ρ_a and ρ_w are the densities of the asthenosphere and water, respectively, and ∇_h^4 is the two-dimensional horizontal biharmonic operator. In equation (2), the effects of the basal load are assumed to be negligible relative to those due to the volcanic load. The permeability of the lithosphere itself is primarily controlled by the sum of the horizontal normal flexural stresses near the surface (where fracturing is most likely to occur¹⁷) given by

$$\sigma_f = -\frac{6D}{H^2}\nabla_h^2 w \quad (3)$$

where H is the elastic lithospheric thickness⁹. (For nearly vertical fractures, only the horizontal stresses need to be considered and hence the vertical compression due to either the plume or the volcanic load is neglected.) Thus, for example, a net compressive stress ($\sigma_f < 0$) acts like an excess confining pressure on magma pathways.

The influence of erosion of fracture walls (due to a combination of melting, thermomechanical erosion, hydrating chemical reactions^{18,19}, and so on) on permeability is controlled by the rate of influx and efflux of net energy due to magma injection. This energy nominally includes all forms of energy that contribute to erosion, for example, heat (for melting and for thermal condition-

ing which facilitates erosion by softening the rock), gravitational potential energy, internal mechanical energy, kinetic energy (for mechanical erosion), and chemical potential energy (for reactive or hydrating effects). The various erosional effects and their interactions are difficult to estimate. Although evidence for melting of wall rock is found in Hawaiian lavas²⁰, it is unlikely to provide the necessary erosion by itself (based on silicate latent heats and estimates of magma heat loss). The loss of gravitational potential energy of magma provides a large source of power for mechanical erosion for which there is evidence in the presence of xenoliths²¹; however, the effectiveness of such erosion is difficult to estimate as it depends on the friability of wall rock, the geometry (such as tortuosity) of the pathways, and many other parameters. However, our model suggests that the formation of discrete islands requires significant net erosion to allow established pathways to remain open in the presence of mounting compressive stresses. Thus, while we cannot quantitatively determine the net erosional effect based on observations and experiments, we do find, *a posteriori*, that the effect must be significant to permit island formation in this model, a prediction that clearly warrants testing with future field and laboratory studies.

Overall, we assume that stress and erosion affect permeability by changing the magma volume fraction (that is, porosity) f due to dykes and cracks. Incremental changes in f are thus assumed to be controlled by increments in net energy and normal stresses

$$Cdf = Bde + d\sigma_p + d\sigma_f \quad (4)$$

where ϵ is the net energy content of the bulk medium (wall rock plus magma) per volume in excess of the far-field value, B is a constant, and C is a hybrid parameter whose inverse C^{-1} represents the responsiveness of crack or dyke volume to stress and erosion (that is, a large value of C causes a small change in f for a given input of energy or stress). We assume that, to first order, $C = C_o/(f(f_{\max} - f))$ which precludes unphysical values of $f < 0$; f_{\max} is the value of f beyond which increases in stress and net energy are partitioned less into changing porosity than into other responses, such as heating or deforming the magma. We assume that this limit is similar to the disaggregation limit for melts, that is, $0.01 \leq f_{\max} \leq 0.1$ (however, f_{\max} need not be evaluated explicitly in this model as it only appears coupled to other parameters). Equation (4) is easily integrated to yield the function $f(\epsilon, \sigma_p, \sigma_f)$. Then, assuming that permeability k is linearly dependent on f , and that, for simplicity, magma percolation obeys Darcy's law, the magma volume flux per area (the Darcy velocity) is given by

$$V = \frac{k_o f_{\max}}{2\mu} \left[1 + \tanh\left(\frac{\sigma_p + \sigma_f - \sigma_o + B\epsilon}{2C_o/f_{\max}}\right) \right] \times \left[(\rho_l - \rho_m)g - (\rho_m h + \rho_a w) \frac{g}{H} \right] \quad (5)$$

where k_o is a reference permeability, μ is the magma viscosity, σ_o is an integration constant representing the intrinsic tensile strength of the far-field lithosphere¹², and ρ_l is lithospheric density. The pressure gradient driving flow (the last bracketed factor in equation (5)) is due to the magma buoyancy, the hydraulic head of magma inside the volcano, and the flexural deflection of lithosphere into the underlying asthenosphere. (If σ_p represents magma overpressurization instead of plume tensile stress, then, strictly speaking, it should be included in the driving pressure; however, this is found to have little significant effect on the final results.)

The volcanic load height h grows according to the ejection rate of magma onto the surface, V ; changes in ϵ are primarily controlled by the injection rate of magmatic net energy, which is also proportional to V . Thus we may write

$$\frac{\partial h}{\partial t} = V = \frac{H}{\Delta Q} \frac{\partial \epsilon}{\partial t} \quad (6)$$

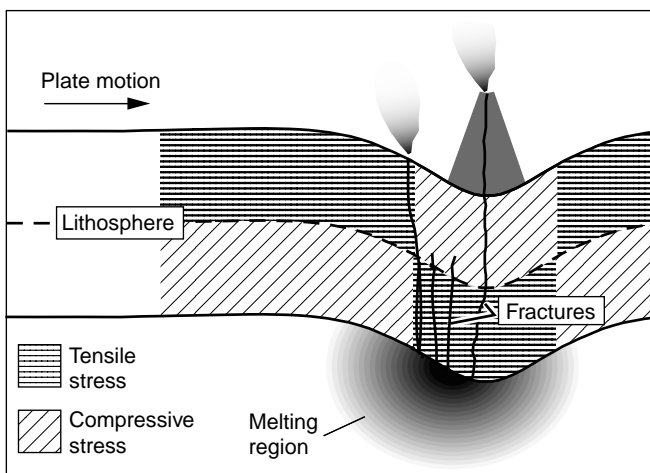


Figure 1 Sketch of the influence of flexural stresses on fracture formation. Fractures form where the magma pressure due to the plume is greater than the sum of compressive stresses due to flexure and the tensile strength of the lithosphere. Once a magma pathway is established, the fracture is kept open in an environment of increasing flexural stresses by erosion of the fracture walls.

where ΔQ is the drop in magmatic energy per volume across the lithosphere (from bottom to top). This final equation provides, first, a description of how h changes with time, t , and second the relation $\epsilon = \Delta Qh/H$ (assuming ϵ and h are both zero at some initial time) which we can then substitute back into equation (5) to eliminate ϵ . The resulting governing equations (1), (2), (3), (5) and (6) with the aforementioned substitutions describe how the rate of change of volcano height h is a strongly nonlinear function of h itself.

Numerical solutions of the governing equations yield chains of discrete volcanoes (Fig. 2) for a wide range of parameters. The first magma pathways form in pristine, unflexed lithosphere, after which a volcanic load begins to grow. The mounting compressive flexural stresses (σ_f) beneath the volcanic load soon overwhelm the tensile stresses (σ_p) from the plume magma source, thereby impeding and eventually precluding the initiation of any further magma pathways in the vicinity of this volcano. However, as the lithosphere moves on, the plume magma source eventually reaches a region of the lithosphere where the flexural compressive stresses are low enough that it can force open new magma pathways to the surface. Erosion provides a positive feedback which keeps established pathways open long enough to form a volcano, even as the compressive flexural stresses grow along with the volcanic load. (The flow in the

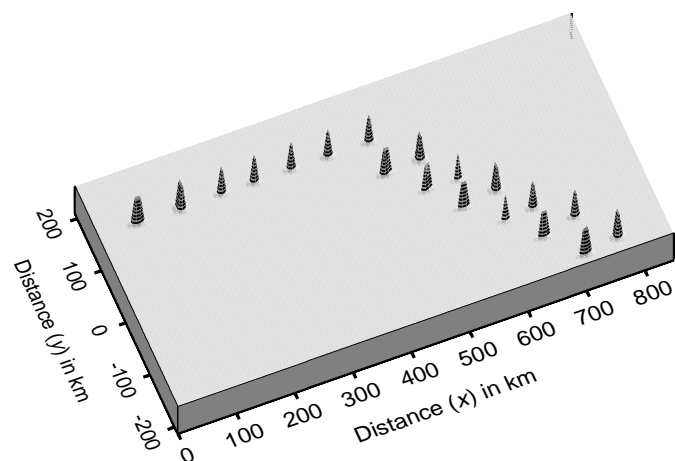


Figure 2 Theoretical model of discrete islands formed on a lithospheric plate moving over a mantle hotspot. In the lithospheric reference frame, the hotspot starts at $x = 70$ km, $y = 110$ km and moves to the right at velocity $v = 10$ cm yr^{-1} , causing a line of single volcanoes. When the hotspot reaches $x = 470$ km, the relative direction of plate motion changes by 45° , causing a transition to a dual line of volcanoes (see text for discussion). The governing equations are solved using a pseudo-spectral code²⁷ with 256×128 Fourier modes. The volcanoes are relatively sharp peaks rather than proper shields because gravity-induced spreading at the surface is neglected. The parameters used to generate the figure are: $D = 2.38 \times 10^{23}$ N m (ref. 9), $H = 30$ km, $\rho_w = 1,000$ kg m^{-3} , $\rho_a = 3,300$ kg m^{-3} , $\rho_m = 2,600$ kg m^{-3} , $\rho_l = 3,400$ kg m^{-3} , $r = 110$ km, $\mu = 100$ Pa s (ref. 13), and $\sigma_o = 5.1 \times 10^7$ Pa (ref. 28). (See text for definitions of symbols.) We choose $\rho = 3$, which results in a plateau-shaped σ_p that facilitates generation of the dual line by providing a wider swath of nearly equal probability of volcano formation; a more peaked function tends to concentrate volcanic edifices on the hotspot axis. Parameter $k_o/f_{\text{max}} = 1.8 \times 10^{-11}$ m^2 is estimated using $F/A_v \approx k_o f_{\text{max}}/\mu(\rho_l - \rho_m)g$, where F is the volume flux of magma (~ 3.6 $\text{m}^3 \text{s}^{-1}$ for Kilauea volcano²⁹), and A_v is the volcano area ($\sim 2,500$ km^2). We choose $A = 5.0 \times 10^7$ Pa, resulting in plume tensile stress or magma pressure that is of the order of the tensile strength σ_o ; and $C_o/f_{\text{max}} = 1.8 \times 10^5$ Pa so that, to be conservative, the minimum resistance to changes in porosity C is also of the order of the tensile strength for plausible f_{max} . The value of $B\Delta Q = 6.3 \times 10^9$ Pa causes the effect of wall-rock erosion to be comparable to or even larger than the flexural stresses, as is a posteriori found to be required for the formation of discrete islands.

established pathways is eventually shut off by the hydraulic head of magma within the volcano itself.) Once the next volcano is established, the process repeats itself. The resulting volcanic spacing λ is proportional to $H^{3/4}$ because the natural length scale of the flexure equation (2) is proportional to $D^{1/4}$ and $D \propto H^3$ (ref. 9). With lithospheric thickness $H = 30$ km (refs 22, 23), we can match the observed volcano spacing of 70 km in the Hawaiian islands¹.

Our simple model predicts that a dual line of volcanoes similar to the Kea and Loa trends of the Hawaiian chain, and comparable trends in other Pacific island chains²⁴, is a natural consequence of the dynamics of the system when it is initiated or perturbed by a volcanic load placed off the hotspot axis, as might occur after a change in tectonic-plate motion. The dual chain occurs because the compressive stresses beneath the off-axis edifice preclude formation of the next volcanoes on that side of the axis; thus, the closest region susceptible to new volcano formation is on the opposite side of the hotspot axis. Subsequent volcanoes form similarly, leading to a chain reaction that results in alternating positions of volcanoes. The eventual separation of the two lines depends on the radius r of the plume magma source; a separation characteristic of the Kea and Loa trends is achieved for $r = 110$ km. This value of r is comparable with estimates of the melt radius (100–150 km) of the Hawaiian plume^{2,8}, which suggests that the plume stress is caused more by a high-pressure melt region than by other sources of plume stress, such as inflation of the hotspot swell (which has a much larger radius¹⁶). However, the spacing between nearest volcanoes is the same as that for the single line, about 70 km. Moreover, the two volcanic lines tend to sample different parts of the plume magma source; this may help explain the disparate geochemistry and petrology of volcanoes on single hotspots as they would arise from regions with different temperatures, degrees of partial melting, and possibly entrainment²⁵.

The present Kea and Loa trends are predicted by our model to be due to an off-axis asymmetry caused by, and perpetuated since, a change in direction of plate motion. As these trends are relatively young, or at least have been strongest in the past 4 Myr, they may reflect a change in plate motion that occurred not 43 Myr ago (the time of the Emperor–Hawaiian bend) but, as recently suggested²⁶ only 3–6 Myr ago. □

Received 8 September; accepted 11 December 1998.

1. Ten Brink, U. Volcano spacing and plate rigidity. *Geology* **19**, 397–400 (1991).
2. Jackson, D. E., Silver, E. A. & Dalrymple, G. B. Hawaiian-Emperor chain and its relation to Cenozoic circumpacific tectonics. *Geol. Soc. Am. Bull.* **83**, 601–618 (1972).
3. Tatsumoto, M. Isotopic composition of lead in oceanic basalts and its implications to mantle evolution. *Earth Planet. Sci. Lett.* **38**, 63–87 (1978).
4. Olson, P. in *Magma Transport and Storage* (ed. Ryan, M. P.) 33–51 (Wiley, New York, 1990).
5. Schubert, G., Olson, P., Anderson, C. A. & Goldman, P. Solitary waves in mantle plumes. *J. Geophys. Res.* **94**, 9523–9532 (1989).
6. Skilbeck, J. N. & Whitehead, J. A. Formation of discrete islands in linear island chains. *Nature* **272**, 499–501 (1978).
7. Ihinger, P. D. Mantle flow beneath the Pacific plate; evidence from seamount segments in the Hawaiian-Emperor chain. *Am. J. Sci.* **295**, 1035–1057 (1995).
8. Vogt, P. R. Volcano spacing, fractures, and thickness of the lithosphere. *Earth Planet. Sci. Lett.* **21**, 235–252 (1974).
9. Turcotte, D. L. & Schubert, G. *Geodynamics* (Wiley, New York, 1982).
10. Guillou, H., Garcia, M. O. & Turpin, L. Unspiked K-Ar dating of young volcanic rocks from Loihi and Pitcairn hot spot seamounts. *J. Volcan. Geotherm. Res.* **78**, 239–249 (1997).
11. Lister, J. R. & Kerr, R. C. Fluid-mechanical models of crack propagation and their application to magma transport in dykes. *J. Geophys. Res.* **96**, 10049–10077 (1991).
12. Rubin, A. M. Propagation of magma filled cracks. *Annu. Rev. Earth Planet. Sci.* **23**, 287–336 (1995).
13. Bruce, P. M. & Huppert, H. E. in *Magma Transport and Storage* (ed. Ryan, M. P.) 87–101 (Wiley, New York, 1990).
14. Lister, J. R. & Dellar, P. J. Solidification of pressure-driven flow in a finite rigid channel with application to volcanic eruptions. *J. Fluid Mech.* **323**, 267–283 (1996).
15. Davies, G. F. Thermomechanical erosion of the lithosphere by mantle plumes. *J. Geophys. Res.* **99**, 15709–15722 (1994).
16. Wessel, P. Observational constraints on models of the Hawaiian hot spot swell. *J. Geophys. Res.* **98**, 16095–16104 (1993).
17. Kohlstedt, D. L., Evans, B. & Mackwell, S. J. Strength of the lithosphere: Constraints imposed by laboratory experiments. *J. Geophys. Res.* **100**, 17587–17602 (1995).
18. Bonatti, E. Not so hot “hot spots” in the oceanic mantle. *Science* **250**, 107–111 (1990).
19. Burnham, C. W. in *The Evolution of the Igneous Rocks* (ed. Yoder, H. S.) 439–482 (Princeton Univ. Press, 1979).
20. Eiler, J. M., Farley, K. A., Valley, J. W., Hofmann, A. W. & Stolper, E. M. Oxygen isotope constraints on the sources of Hawaiian volcanism. *Earth Planet. Sci. Lett.* **144**, 453–468 (1996).
21. Garcia, M. O. Petrography and olivine and glass chemistry of lavas from the Hawaii Scientific Drilling Project. *J. Geophys. Res.* **101**, 11701–11713 (1996).

22. Watts, A. B. An analysis of isostasy in the world's oceans: 1. Hawaiian-Emperor seamount chain. *J. Geophys. Res.* **83**, 5989–6004 (1978).
23. Wessel, P. A reexamination of the flexural deformation beneath the Hawaiian swell. *J. Geophys. Res.* **98**, 12177–12190 (1993).
24. Jackson, E. D. & Shaw, H. R. Stress fields in central portions of the Pacific plate: Delineated in time by linear volcanic chains. *J. Geophys. Res.* **80**, 1861–1874 (1975).
25. Hauri, E. H. Major-element variability in the Hawaiian mantle plume. *Nature* **382**, 415–419 (1996).
26. Wessel, P. & Kroenke, L. A geometric technique for relocating hotspots and refining absolute plate motions. *Nature* **387**, 365–369 (1997).
27. Canuto, C., Hussaini, M. Y., Quarteroni, A. & Zhang, T. A. *Spectral Methods in Fluid Dynamics* (Springer, New York, 1988).
28. Jaeger, J. C. & Cook, N. G. W. *Fundamentals of Rock Mechanics* 3rd edn 190–191 (Chapman & Hall, London, 1979).
29. Swanson, D. A. Magma supply rate at Kilauea volcano, 1952–1971. *Science* **175**, 169–170 (1972).

Acknowledgements. We thank N. Ribe, A. Rubin and Y. Ricard for helpful comments. This work was supported by the NSF.

Correspondence and requests for materials should be addressed to D.B. (e-mail: dberco@soest.hawaii.edu).

A primitive fossil fish sheds light on the origin of bony fishes

Min Zhu*, Xiaobo Yu† & Philippe Janvier‡

* Institute of Vertebrate Paleontology and Paleoanthropology, Chinese Academy of Sciences, PO Box 643, Beijing 100044, China

† Department of Biological Sciences, Kean University, Union, New Jersey 07083, USA

‡ URA12, Laboratoire de Paléontologie, Muséum National d'Histoire Naturelle, 8 rue Buffon, 75005 Paris, France

Living gnathostomes (jawed vertebrates) include chondrichthyans (sharks, rays and chimaeras) and osteichthyans or bony fishes. Living osteichthyans are divided into two lineages, namely actinopterygians (bichirs, sturgeons, gars, bowfins and teleosts) and sarcopterygians (coelacanths, lungfishes and tetrapods). It remains unclear how the two osteichthyan lineages acquired their respective characters and how their common osteichthyan ancestor arose from non-osteichthyan gnathostome groups^{1,2}. Here we present the first tentative reconstruction of a 400-million-year-old fossil fish from China (Fig. 1); this fossil fish combines features of sarcopterygians and actinopterygians and yet possesses large, paired fin spines previously found only in two extinct gnathostome groups (placoderms and acanthodians). This early bony fish provides a morphological link between osteichthyans and non-osteichthyan groups. It changes the polarity of many characters used at present in reconstructing osteichthyan interrelationships and offers new insights into the origin and evolution of osteichthyans.

The fossil fish *Psarolepis romeri*³ was described on the basis of skull and lower jaw materials from the Lower Devonian strata (about 400 million years (Myr) BP) of Qujing, Yunnan, China. Materials assignable to the same genus from the Upper Silurian (about 410 Myr BP) of China⁴ and Vietnam⁵ made *Psarolepis* one of the earliest osteichthyans known so far. The skulls and lower jaws exhibit the overall morphology of sarcopterygians but also show characters found in primitive actinopterygians, such as a tooth-bearing median rostral and a lower jaw with five coronoids (rather than three as in most sarcopterygians)^{3,6}. *Psarolepis* was first placed within sarcopterygians, as a basal member of Dipnormorpha³ or among the basal members of Crossopterygii⁴. The new features revealed by the shoulder girdle and cheek materials reported here (Figs 1d, e, 2, 3) indicate that *Psarolepis* may occupy a more basal position in osteichthyan phylogeny.

Most *Psarolepis* specimens derive from four beds at the same locality in Qujing, the first bed being in the Yulongsi Formation (Pridoli), the second and third beds in the Xishancun Formation (early Lochkovian), and the fourth bed in the Xitun Formation (late

Lochkovian). The specimens described here are from the second and third beds. The shoulder girdles and cheek plates from the third bed are often preserved as internal moulds (Fig. 2a) or as external moulds showing the internal casts of sensory canals and the pore-canal system (Figs 2b, c, 3a). Like elements previously assigned to *Psarolepis*^{3–5}, these materials exhibit the unique ornamentation with large, closely spaced pores on the cosmine surface. This unique ornamentation forms the basis of their assignment to *Psarolepis*, which is also supported by other histological and morphological features and by their association with elements that are directly comparable to the type specimen.

The shoulder girdle (Fig. 2) bears a huge pectoral spine that extends posteriorly from a conspicuous ridge between the ventral and vertical laminae of the cleithrum, resembling the condition in some placoderms and acanthodians. In addition, the symmetrical fin spine⁴ indicates that *Psarolepis* may possess median spines in front of the unpaired fins (Fig. 1a, c), as in sharks and acanthodians. The median fin spine exhibits the same ornamentation as the associated parietal shield and lower jaw⁴; other taxa from the same bed (petalichthyids and galeaspids) cannot possess a similar ornamentation. Such paired and unpaired fin spines are unknown in early osteichthyans, whether sarcopterygians or actinopterygians¹. The only possible exceptions are two questionable Silurian forms, *Lophosteus*, which has indeterminate spine-like fragments⁷, and *Andreolepis*, which has a lateral projection of the cleithrum^{8,9}.

A critical issue is whether *Psarolepis* has the typical sarcopterygian monobasal articulation of the paired fins. Although the internal mould of the endoskeletal shoulder girdle (Fig. 2a) does not show

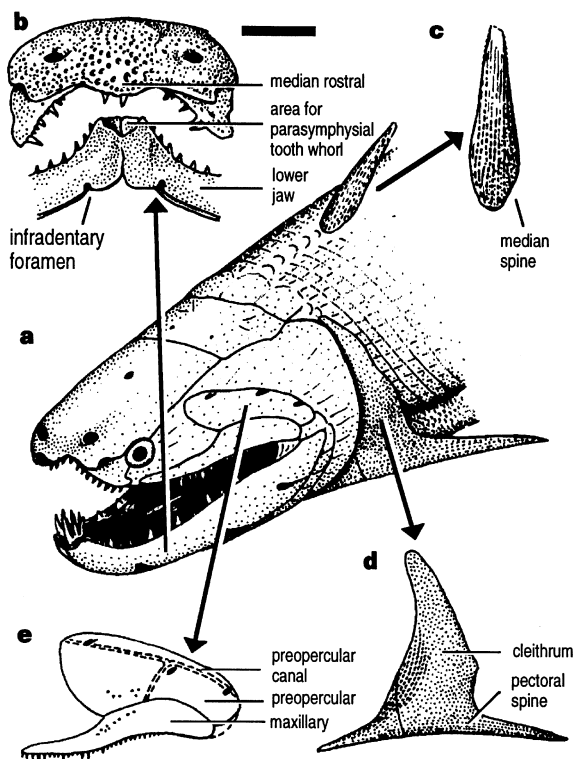


Figure 1 Reconstruction of *Psarolepis*, a 400-million-year-old sarcopterygian-like fish with an unusual combination of osteichthyan and non-osteichthyan features. **a**, Head and anterior part of the fish with tentatively positioned median fin spine. **b**, Anterior view of the skull and lower jaws (from ref. 3). Scale bar, 5 mm. **c**, Median fin spine (from ref. 4). **d**, Shoulder girdle with pectoral spine, based on specimens shown in Fig. 2. **e**, Cheek plate with maxillary and preopercular, based on specimens shown in Fig. 3. Surface ornamentation of the cheek plate is omitted to show the pattern of sensory canals. Most *Psarolepis* specimens derive from four beds at the same locality in Qujing, Yunnan, China.